Three-Dimensional Modeling of Mechanical Forces in the Extracellular Matrix during Epithelial Lumen Formation

Dehong Zeng,* Aldo Ferrari,† Jens Ulmer,‡ Alexey Veligodskiy,†‖ Peter Fischer,§ Joachim Spatz,‡ Yiannis Ventikos,¶ Dimos Poulikakos,* and Ruth Kroschewski†

*Laboratory of Thermodynamics for Emerging Technologies, ETH Zurich, 8092 Zurich, Switzerland; †Institute of Biochemistry, ETH Zurich, 8093 Zurich, Switzerland; ‡Max-Planck-Institute for Metals Research and University of Heidelberg, Department of New Materials and Biosystems, D-70569 Stuttgart, Germany; §Institute of Food Science and Nutrition, Swiss Federal Institute of Technology, ETH Zurich, 8092 Zurich, Switzerland; ¶Fluidics and Biocomplexity Group, Department of Engineering Science, University of Oxford, Oxford OX1 3PJ, United Kingdom; and ‖Molecular Life Science (MLS) PhD program in Zurich, Switzerland

ABSTRACT Mechanical interactions between cells and extracellular matrix (ECM) mediate epithelial cyst formation. This work relies on the combination of numerical modeling with live cell imaging, to piece together a novel nonintrusive method for determining three-dimensional (3D) mechanical forces caused by shape changes of a multicellular aggregate at the early stages of epithelial cyst formation. We analyzed the evolution of Madin-Darby canine kidney cells in 3D cultures using time-lapse microscopy, with type I collagen gel forming the ECM. The evolving 3D interface between the ECM and the cell aggregate was obtained from microscopy images, and the stress on the surface of a proliferating aggregate and in the surrounding ECM was calculated using the finite element method. The viscoelastic properties of the ECM (a needed input for the finite element method solver) were obtained through oscillatory shear flow experiments on a rheometer. For validation purpose, the forces exerted by an aggregate on a force-sensor array were measured and compared against the computational results.

INTRODUCTION

The generation of most multicellular organisms relies on the generation of organs that consist of cells specifically arranged and differentiated to perform essential functions, such as milk production and waste removal in mammalian breasts and kidneys, respectively. One type of functional building block of these epithelial organs is a cyst, a monolayer of polarized epithelial cells enclosing a lumen. How these elaborate multicellular structures are formed from single cells is not resolved (1,2). To understand these complex cell systems, particularly the early stages of cyst formation when a few cells in a proliferating aggregate polarize to form a lumen, one needs to rely on experimental observations on cells in three-dimensional (3D) cultures.

In 3D cultures, the generation of cysts can be recapitulated in vitro using established epithelial cells and defined matrixes (3–5). Living cells in a 3D culture remodel the extracellular matrix (ECM) and vice versa. The morphogenetic outcome is determined by the mechanical interactions between the cells and their surroundings (6–11). An important issue toward understanding the contribution of mechanical forces during cyst formation is to quantify such forces between cells and the ECM at the cellular level. The first necessary step in this direction (before the acquisition and analysis of statistically relevant data) is the development of a methodology for this purpose. Thus we focus on developing such a method in this work.

Various approaches have been proposed to evaluate the mechanical forces between cells and the ECM. Force generated by fibroblasts seeded into a porous matrix contracted the matrix, and the matrix deformations were used to measure the force produced by the cell population. In these studies, one end of the matrix was clamped, and a force gauge was attached to the other end, so that the force produced by the cell population in the ECM was monitored. However, details on forces produced by single cells could not be obtained, except for average values in some cases (12,13). In other studies, cells were deposited on an elastic substrate such as a silicone film. The cells deformed the film and produced wrinkles (14). The force on the substrate was then computed as the product of the wrinkle length and the ''wrinkle stiffness'', which was defined as the force produced by unit length of a wrinkle and calibrated experimentally (15). In addition to wrinkles, micro-beads were utilized to map out the displacements induced by cells in the ECM. For example, cells were plated on top of a layer of collagen attached to underlying polyacrylamide substrate doped with fluorescent micro-beads (16–19). Forces from the cells displaced the embedded beads, but only two-dimensional (2D) displacements were measured, and the forces calculated based on the bead displacements did not reveal 3D information.

Obviously, with cells embedded in a 3D matrix, one needs to gain information about the 3D force distribution. One step toward this direction was the measurement of displacements of the ECM around cells in a 3D culture by tracking visible collagen fibers using 2D differential interference contrast (DIC) images (20). However, the collagen fibers were

Submitted August 29, 2005, and accepted for publication March 3, 2006.

Address reprint requests to Dimos Poulikakos, Laboratory of Thermodynamics for Emerging Technologies, ETH Zurich, Switzerland. E-mail: dimos.poulikakos@ethz.ch.

0006-3495/06/06/4380/12 $2.00

doi: 10.1529/biophysj.105.073494

tracked in only one plane (the in-focus plane of the DIC images). Thus, the subsequent calculation of forces was in 2D, not 3D.

Based on the above, the necessity to further develop methodologies to evaluate the mechanical forces between cells and ECM, in 3D and at the cellular level, is apparent. A 3D computational model is presented herein, aiming at quantifying the mechanical forces between an aggregate and the ECM in 3D during early stages of lumen formation. We used stably transfected Madin-Darby canine kidney (MDCK) cells expressing fluorescently tagged proteins targeting lipid rafts in the plasma membrane. These cells were embedded in collagen gel and a cell aggregate containing three cells was followed by collecting the XY-stacks once every 15 min for 90 min. The XY-stacks were processed to obtain the 3D geometry of the aggregate. A commercial FEM package was used to solve for the force field induced by the shape change of the cell aggregate in the surrounding ECM. Finally, we used a polydimethylsiloxan (PDMS) micropillar sensor array to measure the forces exerted by a cell aggregate on top of the pillars, and applied our computational model to the same setup for validation purpose. The computational results compared well with the measured forces on the pillars.

MATERIALS AND METHODOLOGY

Geometric modeling based on fluorescent images

Cell culture

We used a MDCK clone (YMD cells in the following) stably expressing His-tagged yellow fluorescent protein (YFP) fused to an N-terminal fragment of GAP43 that is targeted to lipid rafts of the plasma membrane. Three-dimensional cultures were obtained by mixing reconstructed soluble collagen type I (Vitrogen, Cohesion Technologies, Palo Alto, CA) with medium containing cells. Trypsinized YMD cells were resuspended in a CO_2 independent medium (Gibco, Invitrogen, Carlsbad, CA) with 1% glutamine, penicillin/streptomycin, and 10% fetal calf serum (FCS), and added to the collagen solution to obtain a final cell density of 1×10^5 cells/ml and a final collagen concentration of 0.4 g/l. A volume of 2 ml of cell-doped collagen was poured in a 3.5-cm glass bottom tissue culture dish previously coated with collagen, incubated for 1 h at 37°C and overlaid with additional 1 ml of cell culture medium.

Microscopy and imaging

The temporal and spatial development of an aggregate was obtained using Deltavision Spectris system (Applied Precision LLC, Issaquah, WA) equipped with an incubation chamber (Solent Scientific Limited, Segensworth, UK), a motorized stage (Nanomotion, Applied Precision), and a cooled charge-coupled device (CCD) camera (CoolSnap HP, Roper Scientific, Duluth, GA). YFP fluorescence was excited at 488 nm and collected in the 510–550-nm optical window. High-resolution XY-stacks of the cells (voxel size, $0.106 \times 0.106 \times 1$ μm) were obtained with an oil immersion objective (60×, 1.4 NA, PlanApo, Olympus, Tokyo, Japan).

Image processing and surface modeling

The XY-stack of fluorescent images of the cell aggregate was deconvolved using the software AUTODEBLUR (Autoquant Imaging, Troy, NY) and imported into an image processing software AMIRA (Konrad-Zuse-Zentrum, Berlin, Germany) for manual segmentation and surface reconstruction, from which a triangulated surface, termed ''the surface mesh'' heretofore, was generated to represent the 3D shape of the aggregate. However, the surface mesh generated in AMIRA was not smooth enough for building a FEM model. Smoothing operations on the surface mesh were performed. Briefly, the rough surface mesh from AMIRA was imported into a geometric modeling package GEOMAGIC STUDIO 6 (Raindrop Geomagic, Durham, NC), to generate a nonuniform B-spline surface (NURBS) that overlaid the surface mesh. Then, a smooth surface mesh was generated using GAMBIT (Fluent, Lebanon, NH) based on the NURBS surface of the aggregate. In one evolution, we recorded the XY-stacks of a cell aggregate (after 24 h in culture) at seven time points, with a 15-min interval, and the NURBS surface and smooth surface mesh were generated for each time point recorded.

Displacement boundary conditions on the surface of a cell aggregate

To obtain the displacements on the boundary of a cell aggregate, we mapped the surface of an aggregate from one time point to the next. Because of the unstructured nature of the surface meshes, the mapping between these two surfaces was not trivial. We performed the mapping using the ''surface warp'' function in AMIRA. Two surfaces at two consecutive times were loaded into AMIRA, and two sets of points termed as landmarks were used, with one set on each surface. A mapping between these two sets of landmarks was first created, and one surface was deformed to match the other using the Bookstein algorithm (21) based on the mapping between the two sets of landmarks, while the connectivity of the deformed surface was maintained. Nodal coordinates of the deformed surface were exported and displacements at any node were obtained by subtracting its old coordinates in the original mesh from its new coordinates in the deformed mesh. These displacements served as boundary conditions in subsequent calculations using the FEM package ABAQUS (Hibbitt, Karlsson & Sorensen, Pawtucket, RI), to obtain the interaction forces between the aggregate and the ECM.

The landmark sets were derived through a ''template matching'' technique in GEOMAGIC. A NURBS surface of an aggregate was composed of many quadrilateral patches mosaiced to represent the aggregate. All these patches, vertices of each patch and the topology of the patches were converted to an entity known as ''patch template'' in GEOMAGIC from the NURBS surface of the aggregate at the first time point, and, through the ''template matching'', the patch template, including the vertices, was warped onto the surface of the aggregate at the next time point. We then exported the vertices of both the original template and the warped template as two sets of landmarks for surface warping between these two time points. On average, there were around 300 vertices in a patch template.

Mechanical properties of collagen gels

The viscoelastic properties of the ECM used in our 3D culture were quantified for computing the stress in the ECM. An ECM made of collagen gel exhibits viscoelastic behavior (11,22). Here, we modeled the collagen gel as a linear viscoelastic material.

Linear viscoelasticity

For a viscoelastic material, the stress at a given time depends not only on the current strain, but also on the deformation history of the material. The constitutive equation of a linear viscoelastic material is written as (23)

$$S_{(t)} = 2\int_{-\infty}^{t} G_{(t-t')} D_{(t')} dt', \tag{1}$$

where $G(t)$ is the relaxation modulus, and $S(t)$ and $D(t)$ are the stress tensor and the strain rate tensor, respectively. The relaxation modulus is assumed

to be a continuous function of time. For viscoelastic solids, the generalized Maxwell discrete relaxation modulus in the following form is used (24,25)

$$G_{(t)} = G_\infty + \sum_{j=1}^{N} G_j e^{-\frac{t}{\lambda_j}}, \quad (2)$$

where G_∞ is the long-term (relaxed) elastic response, λ_j is the relaxation time at one mode of relaxation, and G_j is the corresponding elastic modulus. G_∞, λ_j, and G_j are all constants.

The constitutive model of a linear viscoelastic material is determined through calibrating the constants in the discrete relaxation modulus. Oscillatory shear flow experiments belong to the standard tests for determining these constants. In these tests, the ECM sample is subjected to a harmonic simple shear at different frequencies. In the frequency domain, the generalized Maxwell discrete relaxation modulus is converted to the complex modulus, with its real and imaginary parts being the storage modulus G' and the loss modulus G'', respectively (25),

$$G'_{(\omega)} = G_\infty + \sum_{j=1}^{N} \frac{G_j \omega^2 \lambda_j^2}{1 + \omega^2 \lambda_j^2}$$

$$G''_{(\omega)} = \sum_{j=1}^{N} \frac{G_j \omega \lambda_j}{1 + \omega^2 \lambda_j^2}, \quad (3)$$

where ω is the angular frequency (rad/s), and G_∞, G_j, and λ_j are constants as in Eq.2.

Collagen measurement

We measured the viscoelastic properties of the collagen gel using a rheometer Physica MCR 300 (Anton Paar GmbH, Graz, Austria). The double gap Couette flow chamber of the rheometer was employed to perform oscillation test (frequency sweep). The flow chamber was fixed to the stage and connected to a temperature control unit. After the system was initialized, the temperature of the chamber was adjusted to 37°C and maintained at this level. The collagen gel was poured into the mold and a cylindrical measuring bob, controlled by a computer, was lowered into the chamber. The whole chamber was then covered to prevent dehydration of the gel during incubation. The gel was incubated at 37°C for 1 h before the test was started. Before frequency sweep tests were run, an amplitude sweep test was performed to examine the maximum shear strain below which the gel demonstrated linear viscoelasticity. With this test, we identified the maximum shear strain to be ~12%. A frequency sweep test was then started with a new sample and the storage and loss modulus were measured. The frequencies used were from 0.1 rad/s to 100 rad/s, and the amplitude of shear strain was 3%. The test data were fitted to a two-mode linear viscoelastic model, to calibrate the material constants in the constitutive model of the ECM, as detailed in the Results section. We repeated the frequency test three times, with a new sample of the same concentration prepared each time.

Finite element method

The finite element method was employed to solve for the mechanical stresses in the ECM surrounding a cell aggregate. The FEM mesh in the ECM domain was generated, as detailed below. An input file was created during processing to store all the information, such as the FEM mesh, material properties, initial and boundary conditions, etc. The input file was imported to the solver to start computing the stress distribution in the ECM around an aggregate. A flow chart of the computational model is shown in Fig. 1.

Mesh distortion, remeshing, and interpolation of stress field

A first-order tetrahedral mesh was generated in the ECM domain using a freeware TETGEN (WIAS, Berlin, Germany). A hexahedral domain with

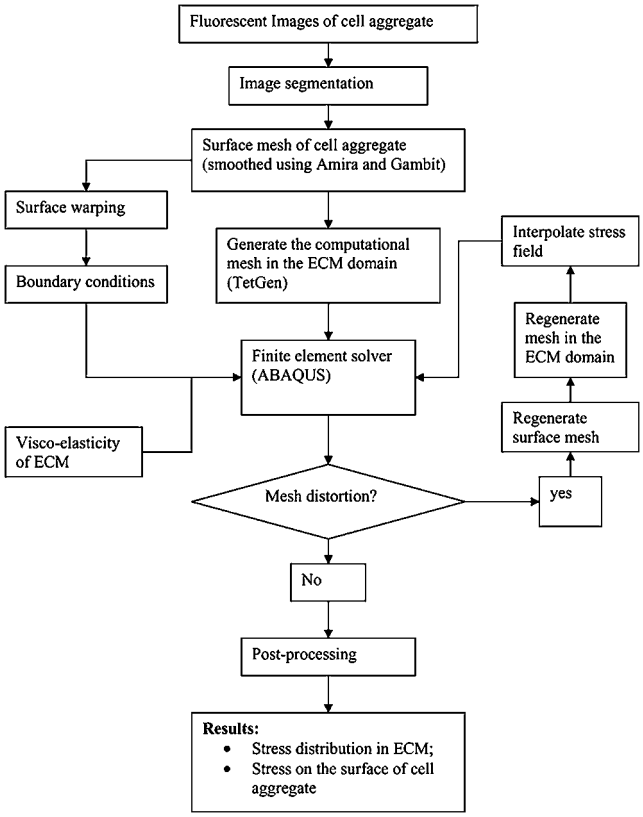

FIGURE 1 Flow chart of the numerical model.

dimensions of 40 × 40 × 30 μm was taken as the computational domain, while the surface mesh representing the cell aggregate specified the inside boundary of the computational domain (Fig. 2). The glass coverslip was 1 μm beneath the hexahedral computational domain.

The mesh might become highly distorted during the simulations, causing the FEM solver to diverge. Before this occurs, a new mesh was generated on the deformed domain, and the solutions on the old mesh were interpolated onto the new mesh as initial conditions for restarting the simulation using the new mesh. For a point P in the new mesh, one element, E_p, of the old mesh containing P was identified through a searching algorithm, and the local coordinates of the point P on element E_p were computed. The value of an interpolated field variable at P was then calculated as

$$f_p = \sum_{i=1}^{4} \phi_i(\xi_1, \xi_2, \xi_3) f_i, \quad (4)$$

where f_p is the interpolated value of a field variable at the point P in the new mesh, f_i is the nodal value of the same field variable in the old mesh, ϕ_i are shape functions, and ξ_i, $i = 1,2,3$, are local coordinates of P on the element E_p. The field variables could be components of displacements or stresses. In our simulations, we interpolated stress values from the old mesh.

The interpolation was straightforward, but the CPU cost in performing the searching on an unstructured mesh was significant. It was prohibitively expensive to do the search on the entire domain. To minimize the computational cost, the following technique was applied to implement the searching algorithm: a structured hexahedral mesh was created in the ECM domain, underlying the unstructured mesh. The nodal spacing of the hexahedral mesh was equal to the average nodal spacing of the old mesh. Elements of the old mesh that were on a hexahedral element or in a small region near it were identified and stored, and these elements were said to be linked with the hexahedral element. The number of tetrahedral elements linked to a hexahedral element was about a few hundred on the average, far

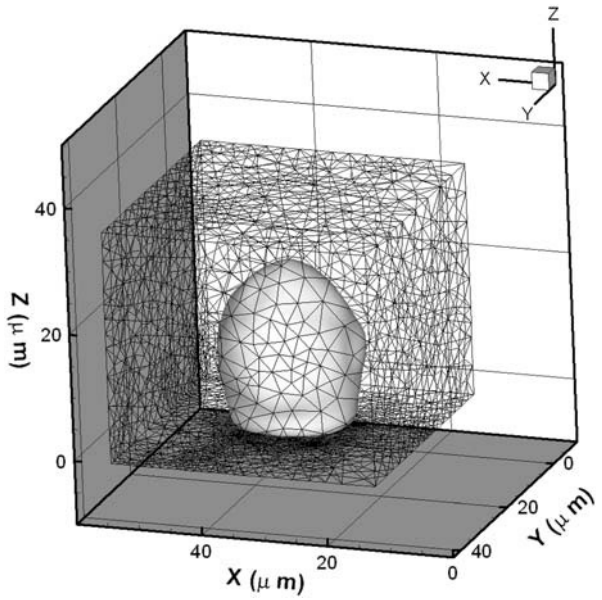

FIGURE 2 A tetrahedral mesh generated using TetGen. The meshed domain is the ECM space outside an aggregate, with the aggregate represented by the shaded object. From the aggregate surface (*shaded object*) to the outside surface, the mesh is coarsened.

less than the total number of elements in the mesh. Before starting the search, the hexahedral element in which a point P resided was first computed. With the structured hexahedral mesh, the computation was fast. The search was then limited to the tetrahedral elements linked with the particular hexahedral element containing the point P, thus minimizing the computational cost.

Postprocessing of the simulation results

We were interested in the stress distribution on the surface of a cell aggregate, as well as the stress distribution in the ECM. When a simulation was successfully completed, we extracted the stress data from the output file, and calculated the stress distribution on the surface of the aggregate. The stress at one point on a surface is calculated as

$$t_i = \sum_{j=1}^{3} n_j \sigma_{ij} \quad i = 1,2,3, \tag{5}$$

where t_i, $i = 1,2,3$, are the components of the stress vector, n_j, $j = 1,2,3$, are the components of the unit normal vector at the point on the surface, and σ_{ij} are components of the Cauchy stress tensor.

Knowing the stress at each point on the surface of an aggregate, we were then able to calculate the total force on a cell aggregate, defined as

$$\vec{F} = \oiint \vec{t}\, ds, \tag{6}$$

where the integration was performed over the entire surface of the cell aggregate.

In addition to the stress, the distribution of von Mises stress was also examined during the postprocessing. The von Mises stress is a function of the stress components. It is used to generalize the uniaxial yield criterion for testing plastic deformation of a material. The von Mises stress is defined as

$$\sigma_v = \sqrt{\frac{1}{2}[(\sigma_1 - \sigma_2)^2 + (\sigma_2 - \sigma_3)^2 + (\sigma_3 - \sigma_1)^2]}, \tag{7}$$

where σ_1, σ_2, and σ_3 are principal stresses of a stress tensor σ_{ij}.

Mesh dependency test

To perform a mesh dependency test, we computed the stress distribution for a gradually refined series of meshes and examined the von Mises stress along a closed curve around a cell aggregate. We chose to examine the stress on the cell aggregate surface because the gradient of stress in this region was higher than that in other regions.

Typical results of the mesh dependency test are shown in Fig. 3. Four successively refined meshes were used in the test, including a coarse mesh (122,963 elements, 23,312 nodes), a medium mesh (269,505 elements, 51,834 nodes), a medium-fine mesh (412,950 elements, 81,275 nodes), and a fine mesh (812,168 elements, 157,872 nodes). The von Mises stress at 200 points on the selected curve around the cell aggregate was examined. Between the coarse and the fine meshes, the average difference in von Mises stress was 11.7%. Between the medium and fine meshes, the average difference was 5.4%, whereas an average difference of 2.6% was calculated between the medium-fine and fine meshes. Based on these results, we used the medium-fine mesh for the simulations.

Measurement of mechanical forces at the cell-ECM boundary using a force sensor array

To evaluate the accuracy of our computational model, we measured the mechanical force exerted by a cell aggregate on a force sensor array made of PDMS micro-pillars inspired from the system of Tan and co-workers (26). The force sensor micro-array was produced following standard lithographic techniques (27). Briefly, a negative replica of the pillars was produced using SU8-10, a standard negative photoresist (Microchemicals GmbH, Berlin, Germany). The lithographic process was preformed on a mask aligner (MJB-3, Karl Suess MicroTec Lithography GmbH., Garching, Germany) and with a chromium mask, written on a Maskwriter (DWL-66, Heidelberg Instruments Mikrotechnik GmbH., Heidelberg, Germany). After the mold preparation, PDMS (Sylgard 184, Dow Corning, Midland, MI; base to cross-linker mixing ratio 10:1) was poured over the mold and was degassed for 1 h at 5×10^{-2} mbar. The mold was mounted on coverslips (24 × 24 mm, Carl Roth GmbH, Karlsruhe, Germany) and cured at 65°C for 12 ~ 14 h. The stiffness of the pillars (199.88 N/m for pillars of 10 μm in height, 5 μm in diameter) was obtained using a calibrated AFM cantilever.

The tips of the pillars were coated for 2 min with type I collagen at a final concentration of 100 μg/ml. After rinsing with PBS, the samples were mounted with vacuum grease on a punched 6-cm petri dish and UV-sterilized for 2 min.

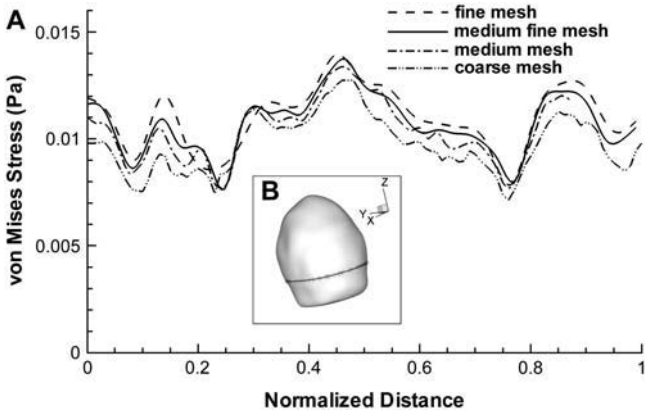

FIGURE 3 Mesh dependency test results. The horizontal axis is the normalized distance along a curve surrounding the aggregate (*A*). The selected curve around the aggregate is shown in the inset (*B*) where the shaded object represents the cell aggregate.

Single YMD cells were seeded on top of the micro-array at a density of 12.5×10^3 cells/ml. After the cells were attached to the pillar array, the sample was overlaid with 500 μl of 50% growth factor reduced Matrigel (Becton-Dickinson Bioscience, San Jose, CA).

The time-lapse recordings of YMD cell aggregates on collagen-coated micro-pillars were obtained using a wide-field inverted fluorescence microscope (IX71, Olympus, Hamburg, Germany) equipped with an incubation chamber and a motorized stage (Nanomotion, Applied Precision LLC). Images were recorded every 30 min over 2.5 h, using a cooled CCD camera (CoolSnap HQ, Photometrics, Trenton, NJ) and a 40× long distance objective with a resulting pixel size of 165.6 × 165.6 nm. The pillar bending was imaged in phase contrast at the tip of the pillars.

Analysis of pillar movement was preformed using IMAGE J. The entire image stack was first aligned to eliminate thermal drift during image acquisition. Then the center of mass of individual pillars in the array was measured for each image. As reference for zero deflection, an image of the pillars without cell aggregate was aligned and analyzed in the same manner. After subtraction, the resulting force was calculated with an accuracy of ~10 nN based on the pillar stiffness and bending.

RESULTS

Forces on micro-pillars: model validation

Well-polarized cysts developed on the pillar array after 72 h. Confocal sections were taken to confirm visually that they were attached to the micro-pillars. The forces exerted on 106 pillars underlying the cyst were experimentally determined and varied from 20 to 230 nN among the pillars (Fig. 4, *A* and *B*). We built a computational model of the pillar array following the method described in the previous section. Briefly, the surface meshes of the cyst were reconstructed based on the XY-stacks at the first two time points, and displacements at the cyst-pillar interface were derived with surface warp using AMIRA. These displacements were imposed as the boundary conditions at the cyst-pillar interface and the forces in the pillars were calculated using ABAQUS. A comparison of the calculated against the measured force is shown in Fig. 4 *D*, along with the location of each pillar (Fig. 4 *C*). The maximum difference is 36% (pillar 87), with an average difference of 8.3%. At most pillars, the computed forces were lower than the measured forces, indicating that the computational model underestimated the forces between the cyst and the ECM.

The assumption on the contact condition between the cyst and the pillars could be one source of error. In the computational model, no relative motion at the cyst-pillar interface was assumed. It was not clear if there was sliding on the interface, and investigating the contact conditions between the cyst and the pillars was beyond the scope of this project. The surface warping performed using AMIRA could also contribute to the discrepancy.

Collagen viscoelastic properties

We measured the storage modulus of the ECM (Fig. 5). At frequencies higher than 6 rad/s, the accuracy of the measurement degenerated because of the inertia effect of the measuring system, therefore we excluded the data at frequencies higher than 6 rad/s. The storage modulus obtained here was comparable to that in a previous study (11).

The measured storage modulus values were regressed by the following equation

$$G'_{(\omega)} = G_\infty + \frac{G_1\omega^2\lambda_1^2}{1+\omega^2\lambda_1^2} + \frac{G_2\omega^2\lambda_2^2}{1+\omega^2\lambda_2^2}, \quad (8)$$

which included the first three terms of the storage modulus G' in Eq. 3. The two-mode model in Eq. 8 was appropriate for describing the mechanical behavior of the collagen gel within the tested frequency range. An example of such regression is shown in Fig. 5 *A*. The shear modulus and relaxation times derived from the above regression are also shown in the figure (table in panel *B*). It is noted that the relaxation time is of the order of a few seconds, which is negligible compared to the long time of observation during lumen formation (15 min up to 1.5 h). This implies that the stress in the ECM is dominantly determined by long-term response of the collagen gel, characterized by the relaxed shear modulus G_∞.

Stress distribution

Single YMD cells embedded in collagen developed over time into complex 3D structures. An evolution of an aggregate containing three cells in the culture is shown in Fig. 6 *A*. Our numerical model applies to cell evolutions of arbitrary shapes and sizes. Here we present the results from the simulation of the evolution presented in Fig. 6, a critical morphological event during cyst formation, namely lumen formation. The surfaces representing the boundary between the aggregate and the ECM were reconstructed from fluorescent images (Fig. 6 *B*). The aggregate developed in 3D partially touching a thin layer of collagen (1 μm in thickness) fixed to a glass surface. This proximity to a rigid surface likely caused the lower part of the aggregate to flatten. There was little change in the center of mass of the aggregate, but the entire aggregate deformed and rotated during the time of observation.

The simulation was started with the assumption that there was initially no stress in the ECM, and stopped at the seventh time point (90 min). The boundary displacements were specified on the surface of the cell aggregate, whereas the outside boundary was fixed. Remeshing was performed at each time point of observation.

We examined the 3D distribution of tangent, normal, and von Mises stresses on the surface of the aggregate at different times (Fig. 7). With our computational model, we calculated the stress distribution on the surface of the cell aggregate at any time throughout its evolution. It is noted that the stress distribution is strongly heterogeneous on the interface between the cells and the ECM at any time. This demonstrates

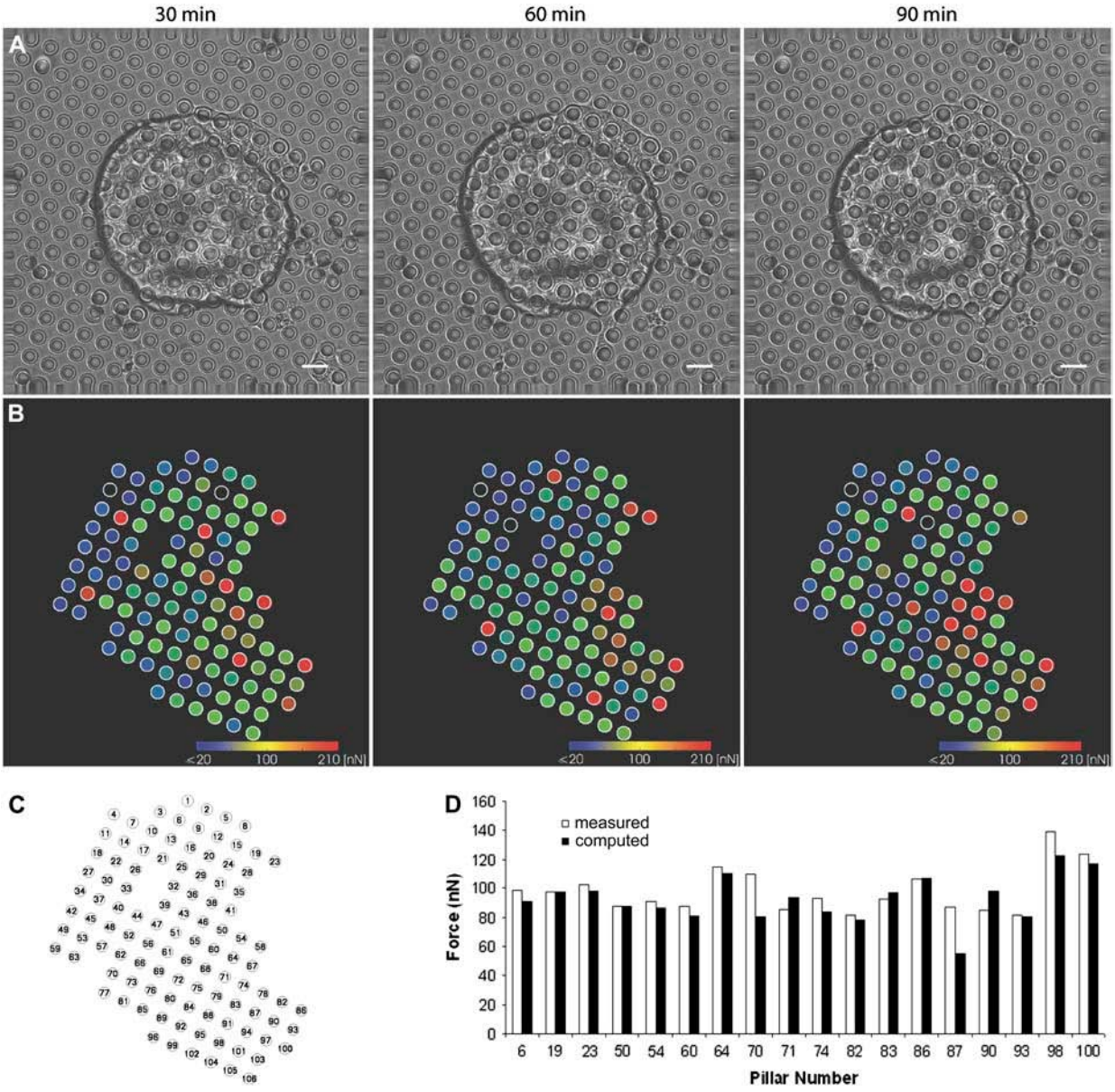

FIGURE 4 MDCK cyst on top of micro pillars. (*A*) After 4 days, a cyst developed on pillars. XY-stack images were taken every 30 min over a period of 2.5 h. Images of the cyst and pillars at the cyst-pillar interface are shown here for three time points. The scale bar in each panel is 10 μm. (*B*) contour plots of the measured forces on the pillars corresponding to the three time points shown in the upper row. (*C*) Pillar arrangement showing the location of the pillars, numbered from 1 to 106. (*D*) Comparison of computed forces at 60 min against the measured forces at some pillars. Shown in this figure are the pillars experiencing forces higher than 80 nN. With pillars experiencing forces larger than 20 nN, the average difference is 13.5%. We excluded the pillars experiencing forces below 20 nN because the estimated accuracy of the measurement was ~10 nN.

the 3D nature of the mechanical interaction between cells and the ECM. Such stress patterns cannot be properly captured using a 2D model. There is considerable variation in the magnitude of the mechanical interaction between the cells and the ECM through the reported evolution. Increased mechanical force is the result of cell shape change causing increased level of compression and/or stretching on the ECM. There is gradually elevated stress concentration (von Mises) near the bottom of the aggregate, due to the proximity of the solid glass boundary. Interestingly, tangential and normal stresses distributions seem to complement each other, with the tangential stress concentrating more at the right side than the left side of the aggregate, while the normal stress demonstrates the reverse pattern. Rotation of the aggregate could be related to the stress pattern observed here.

The stress distribution inside the ECM was also examined. We visualized the 3D distributions of stress by extracting data in three cross-sectional planes through the ECM domain (Fig. 8). The stress within the ECM was also highly heterogeneous, and high stress was localized at the region

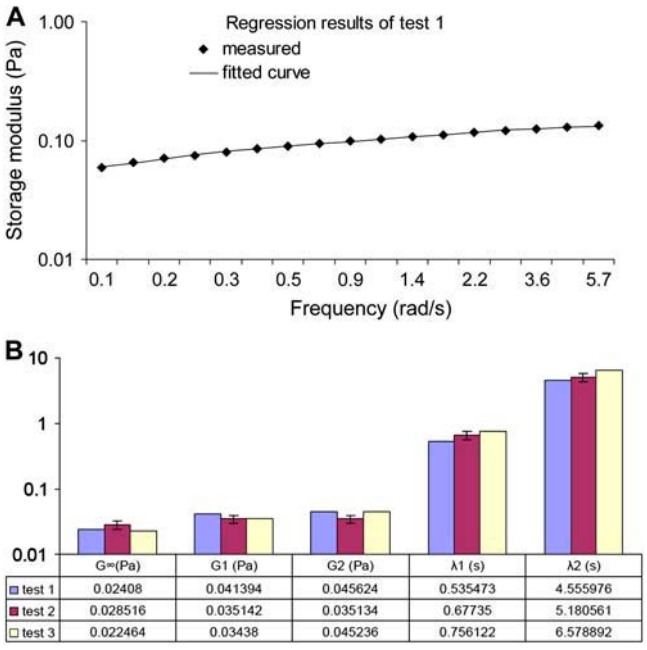

	G∞(Pa)	G1 (Pa)	G2 (Pa)	λ1 (s)	λ2 (s)
test 1	0.02408	0.041394	0.045624	0.535473	4.555976
test 2	0.028516	0.035142	0.035134	0.67735	5.180561
test 3	0.022464	0.03438	0.045236	0.756122	6.578892

FIGURE 5 The measured storage modulus was fitted to Eq. 8 to derive the constants in the discrete relaxation modulus. (*A*) An example of the curve fitting for the sample polymerized for 1 h, with a concentration of 0.4g/l. (*B*) Bar chart of shear moduli and relaxation times from three tests along with the error bars. The error bars indicate the mean ± SE of each parameter from the three tests. Values of the parameters are shown in a table right beneath the bar chart.

close to the cell-ECM interface. The stress patterns evolved with time, due to changes in the shape of the aggregate. The ECM in contact with the aggregate was deformed and displaced, producing stress at the interface between the cell and the ECM, as well as inside the ECM. What we cannot accommodate in our consideration at this stage is the degradation of collagen and thus the possibility of regions with stress reduction. Thus we are overestimating the realistic forces in the ECM. The stress reached a limited region into the ECM. This pattern is reminiscent of what is described by the well-known Saint-Venant's principle in elasticity theory, which states that local deformations and forces in an elastic body stay local (24). The proximity the glass coverslip near the lower part of the aggregate caused high stress in this region. The total force on the aggregate surface as defined in Eq. 6 was calculated, and its magnitude versus culture time is shown in Fig. 9. The total force increased during the recorded evolution because the aggregate was compressing and/or stretching its boundary more and more as it developed. The total force increased initially (between 15 and 30 min), decreased temporarily (between 30 and 45 min) and increased thereafter continuously for the rest of the evolution. It is unresolved why the 30-min value is extremely high or why a sudden decrease of the total force until 45 min was observed. It might be that the force peak at 30 min reported about a special event during lumen formation. However, more simulations need to be performed on different evolutions to establish first the reproducibility of the phenomenon and then a hypothesis.

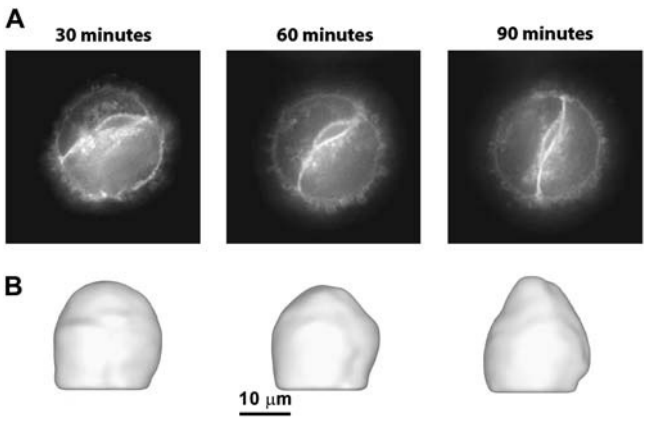

FIGURE 6 Cyst development in 3D collagen culture. (*A*) Fluorescence (XY slice) from the middle section of Z-stacks performed at 30, 60, and 90 min from the start of recording. (*B*) 3D surfaces reconstructed from fluorescent images, representing the cell aggregate in culture at the three times. The collagen gel outside the aggregate is not shown. The aggregate sits on top of a collagen-coated glass coverslip. The scale bar corresponds to 10 μm.

In summary, we demonstrated that a reliable approximation of 3D forces acting on evolving surfaces can be obtained with our method. The obtainable details about the contribution of the different stress components, the total force, and unit volume force depend strongly on the spatial and temporal resolution of the images and bear thus great potential for follow-up analyses.

DISCUSSION AND FUTURE WORK

We established a nonintrusive method for quantifying the 3D mechanical interactions between a cell aggregate and the ECM. Our method is guided by fluorescent live cell imaging, which is a substantial improvement compared to studies where cells are simplified as polygons (28), polyhedra (29), ellipsoids (30), or rods (31). In this work, geometric fidelity of the computational model is pursued through geometric modeling based on fluorescent time-lapse images, which bears several advantages.

First, the fluorescent images were obtained on live cells, allowing the computational model to capture the actual shape of the cells in a realistic time sequence. Despite the fact that live cell imaging of 3D epithelial cells in culture presents many intrinsic challenges, we succeeded in recording the initial stages of lumen formation, a key event during cyst formation(1,2,32,33). High temporal resolution of the recordings was achieved, allowing detailed analysis of the spatial and temporal parameters regulating evolution toward lumen formation (A. Ferrai, A. Veligodskiy, D. Zeng, and R. Kroschewski, unpublished data).

Second, the use of fluorescent cells allowed us to detect the entire plasma membrane of the proliferating cells and to

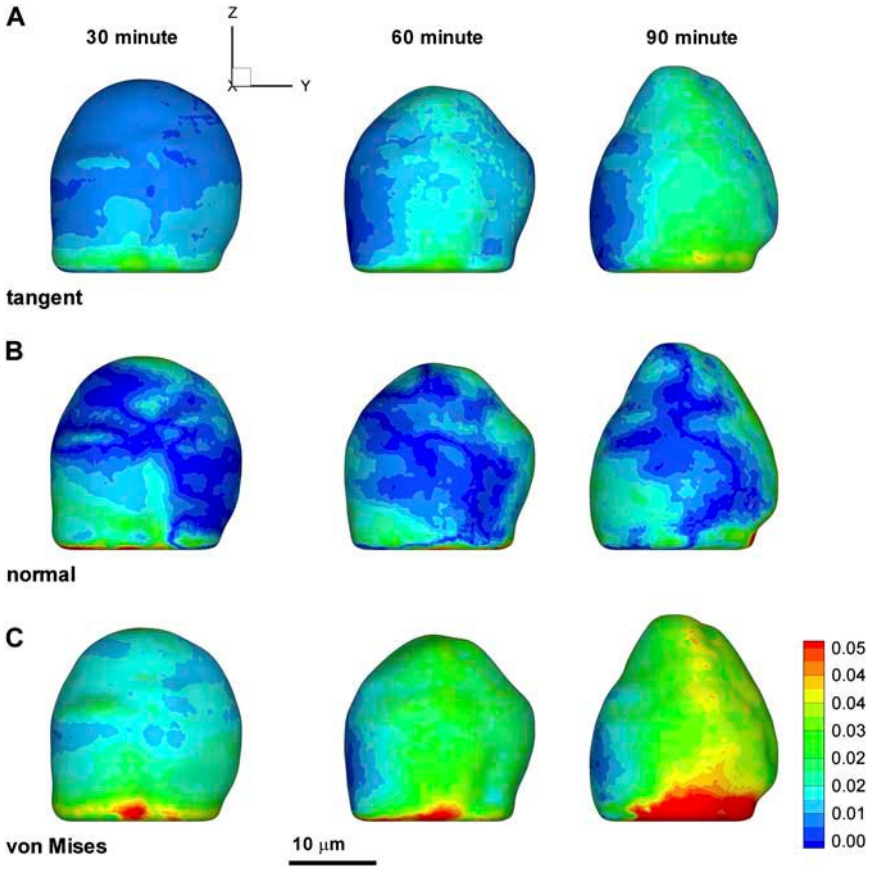

FIGURE 7 Stress distribution on the surface of the aggregate at three time points during one evolution (30, 60, and 90 min). The time in the culture is labeled in column. (*A*) Magnitude of stress in the local tangent direction of the aggregate surface. (*B*) Magnitude of stress in the local normal direction. (*C*) von Mises stress on the surface. Note that the same view and contour levels are used in all the panels. Unit of the stress is Pascal. The scale bar near the bottom corresponds to 10 μm.

obtain a complete and detailed 3D representation of the evolving aggregate. This was in striking contrast to a previous 3D study where only DIC images were analyzed and thus only 2D images and force fields were derived (20). Quantitative analysis and 3D geometrical reconstruction using DIC images is extremely difficult due to the nonlinear relationship between the geometry of the objects and the intensity of the images (35). For these reasons, DIC imaging has been restricted to 2D applications, or 3D applications where the shape of cells is assumed to be symmetrical (36). The 3D geometry of a developing aggregate is largely unpredictable and nonsymmetric, therefore assumptions on symmetry cannot be made for our experimental system (Fig. 6 *B*).

Finally, computational models combined with experimental input are powerful tools in studying the mechanical interactions of evolving cells in 3D space. With a computational model, changes in geometry, boundary conditions, and material properties can be properly accommodated. In this work, we developed an FEM model to evaluate the mechanical forces between cells and the ECM during lumen formation. The solution for the force field in the ECM was obtained with the input from experiments defining the time-dependent geometry of the cell aggregate and mechanical properties of the ECM. We tested the accuracy of an adapted computational model against experimental force measurements based on a micro-pillar array. The computational results were ~8% different from the experimental data on the average (Fig. 4 *D*). Given the complexity of the problem, this agreement was deemed satisfactory. The discrepancy could result from improper assumption on the contact conditions between the cyst and the pillars.

Thus, our work provides a validated approximation of the forces in 3D cell-ECM interactions. Obviously, this method is applicable not only for the biological system presented here but also for other living systems where the changes of the cell shapes can be obtained and the mechanical properties of the surroundings can be determined.

This work brings in some speculations on the effects of mechanical forces on lumen formation. In addition to ECM secretion and degradation, cells embedded in the ECM cause compression and stretching of the fiber network as they grow. It is possible that the mechanical feedback regulates the sequence of morphological events, and hence lumen and cyst formation. Mechanical properties of the ECM are known to determine the molecular responses of individual cells and therefore the cell fate (37,38). To further explore this aspect, we investigated the effects of ECM rigidity on lumen formation by examining the initial stages of lumen formation for cell aggregates proliferating in collagen gels of different rigidity, as detailed in the Appendix. Our results suggest that lumen formation is delayed by increasing the stiffness of the ECM. Different levels of mechanical

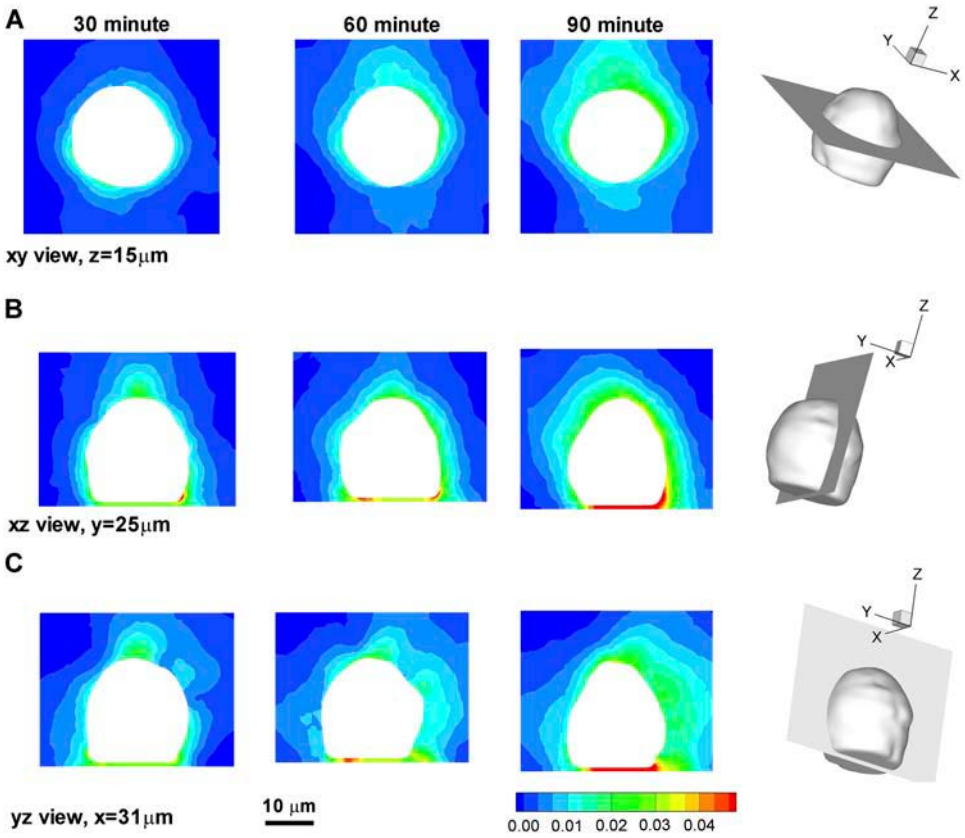

FIGURE 8 von Mises stress distribution within the ECM domain at three time points during one evolution (30, 60, and 90 minutes). (*A*) von Mises stress distribution in a plane through the ECM domain. The section plane is perpendicular to the *Z* axis, as indicated in the rightmost panel of row *A*. (*B*) von Mises stress in a section plane perpendicular to the *Y* axis. (*C*) von Mises stress in a section plane perpendicular to the *X* axis. Unit of the stress is Pascal. The same contour levels are used for each row. The scale bar corresponds to 10 μm.

interactions exist because of the variations in the rigidity of the ECM, and the experiment results indicate that mechanical forces could play a role in affecting the spatial configuration of the cells in an aggregate, including the lumen formation.

Developing cell aggregates assume different 3D configurations. For example, the reconstructed 3D geometry of the aggregate reveals a flattened surface near the glass coverslip, whereas the upper surface is elongated upward. It has been suggested that the cells adjust their shapes and relative locations under the influence of surface mechanics (39). We may therefore postulate that cellular activities, such as membrane trafficking, cytoskeleton contractions, etc., cause continuous changes in mechanical forces at the surface and inside the cells, which in turn contribute to the continuous evolution of the cell shapes and aggregate configurations. The configuration changes of an aggregate that we observed in 3D culture could be just the result of this dynamic adjustment to the mechanical forces over a long period of time, and lumen and cyst formation is the outcome of the adjustment to the changes in mechanical forces in which an energetically stable state is reached. Therefore, it is a logical next step to investigate the contribution of surface micromechanics in regulating cell aggregate configurations and lumen formation, as well as the cellular mechanisms that could affect the surface mechanics and the mechanical conditions within the cells during lumen formation. In addition, there must be some other forces that balance the force caused by cell shape change. For example, surface tension, viscous drag, and focal adhesion might be the factors that should be considered to obtain a complete picture of the mechanical interactions between the cells and the ECM.

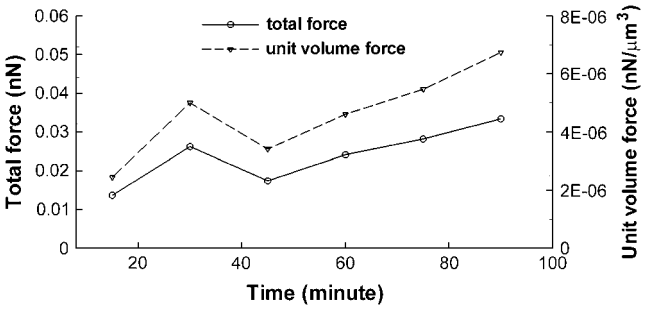

FIGURE 9 Magnitude of the total force on the aggregate versus observation time.

To form a cyst, individual cells in a cell aggregate have to coordinate proliferation, migration, growth, exocytosis, polarization, and shape changes (2). Our approach of combining FEM modeling with live cell imaging represents a first step toward quantifying the mechanical interactions between cells and ECM during epithelial lumen formation. The computational model developed in this work provides a quantitative approximation of a part of this complex biological

process. Future studies are required to interpret the biological importance of the mechanical forces during epithelial morphogenesis, opening new possibilities in materials science, tissue engineering, and biology.

APPENDIX

We are interested in understanding the conditions leading to lumen formation between several epithelial cells. In addition to soluble growth factors and nutrients, molecular composition, density, and rigidity of the ECM define tissue specific microenvironments that in turn influence cellular differentiation, proliferation, and survival. Single MDCK cells embedded in a collagen matrix sense local density and mechanical response of collagen fibers to choose between 2D and 3D growth. Moreover collagen type I networks with different structural properties modulate both size and shape of the resulting MDCK 3D evolutions.

We describe here the experiments and statistical analyses performed to investigate the influence of ECM rigidity on lumen formation. In these experiments, we used collagen gels jellified for 1 and 2 h to achieve different rigidity in the ECM. Collagen rigidity was quantified by the relaxed shear modulus and measured on the rheometer as described previously.

Materials and method

Cell culture and microscopy

To prepare specimens for confocal microscopy, YMD cells were plated in collagen gels of 1.6 cm in diameter. The gels were detached from plastic immediately after collagen jellification. After 4 days of growth, the cells were formaldehyde-fixed and immunostained with 3F2 antibodies against an apical transmembrane protein gp135 (40) and nuclei were stained with Hoechst 33258, as described in Pollack et al. (41). Briefly, the cells were fixed in 4% formaldehyde, permeabilized with 0.025% saponin, washed with 75 mM NH4Cl, 20 mM glycine, blocked in 10% goat serum, 0.025% saponin, and incubated with primary antibodies and secondary antibodies labeled with AlexaFluor594 (Molecular Probes, Eugene, OR) overnight at 4°C on a rocking plate; all antibodies were diluted in 10% goat serum, 0.025% saponin. PBS1 buffer (138 mM NaCl, 2.7 mM KCl, 10 mM Na2HPO4, 1.75 mM KH2PO4, 1 mM CaCl2, and 0.5 mM MgCl2) was used in all solutions to preserve cell-cell contacts. Gels were mounted on glass slides in Mowiol, diazabicyclo [2,2,2]octane (DABCO) and air-dried before imaging. Unless stated otherwise, all chemicals were obtained from Sigma (St. Louis, MO).

Stained YMD cell aggregates were examined with a Leica SP2 AOBS confocal microscope (Leica Microsystems AG, Solms, Germany), with the presence of a resolvable lumen checked and the number of cells in an aggregate counted (Fig. 10, *A* and *B*). All the images were collected using an oil immersion high resolution objective (63×, 1.4 NA, HCX Plan APO; Leica Microsystems). Per condition, around 300 cell aggregates, with the number of cells in an aggregate ranging from 2 to 20, were analyzed.

Statistical analysis

We grouped the cell aggregates according to the number of cells contained in each aggregate. Some aggregates contained a lumen, some did not, while the rest could not be positively identified with regard to the existence of a lumen (Fig. 10, *A* and *B*). We counted each type aggregates, and calculated the probability of lumen formation as $(N_L + 0.5N_{UC})/(N_L + N_{UC} + N_{NL})$, where N_L, N_{NL}, and N_{UC} were, within each group, the number of aggregates with a lumen, ones without a lumen, and those in which lumen existence was uncertain, respectively. The probability of lumen formation was plotted as a function of the number of cells in an aggregate (Fig. 10, *C* and *D*). The probability data were fitted with a two-parameter statistical function using Origin 7.5 SRI (OriginLab, Northampton, MA):

$$y = E_f \times [1 - e^{-K(x-1)}], \tag{9}$$

where x was the number of cells in an aggregate, y was the probability of lumen formation, and E_f and K were two constants. E_f was the efficiency of lumen formation, i.e., the asymptote of the probability curve, and K indicated the change rate of the probability versus the cell number. The higher value of K implied faster lumen formation requiring less number of cells. To express this concept on the parameter K directly, we defined $c_{1/2}$ as

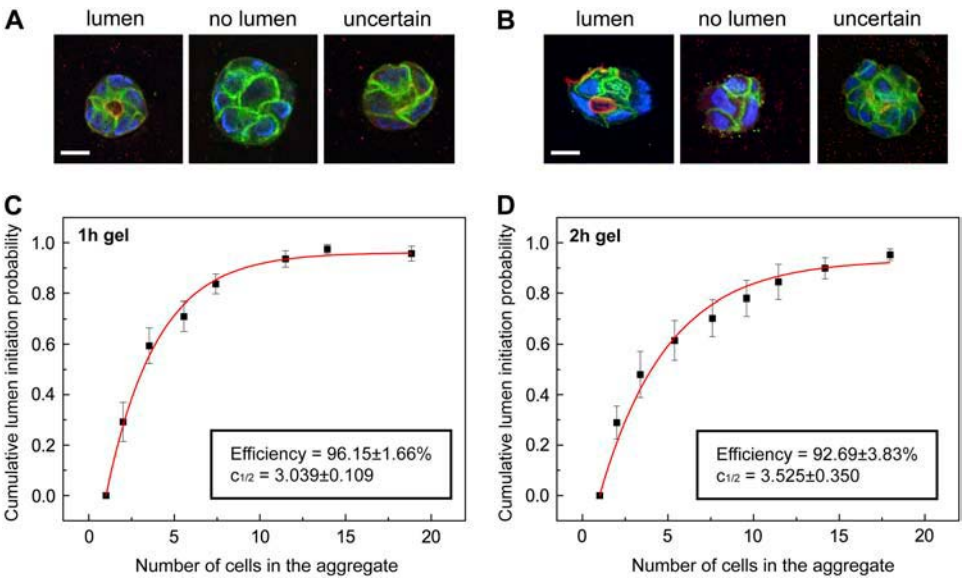

FIGURE 10 Matrix rigidity modulates cell-number dependency of lumen initiation. (*A*) Typical confocal images of three categories of aggregates in the ECM with 1 h jellification time (YMD samples): lumen; no lumen; or where the presence of a lumen is uncertain. Localization of gp135 (*red*), of nuclei (*blue*), and the YFP fluorescence (*green*) of a central section is depicted. (*B*) Corresponding categories for 2 h jellification YMD aggregates. Scale bar corresponds to 10 μm. (*C–D*) Cumulative lumen initiation probability is reported as function of the number of cells in the aggregate for YMD cells cultured in a soft (collagen, 2 g/l, 1 h jellification, 300 aggregates) and rigid ECM (collagen, 2 g/l, 2 h jellification, 300 aggregates). Data points are reported as black squares, error bars correspond to the calculated mean ± SE. Calculated efficiency and $c_{1/2}$ values are reported with the relative errors as insets in the graphs.

$$c_{1/2} = 1 + \frac{\ln 2}{K}, \tag{10}$$

which was the number of cells when the probability of lumen formation was half of the efficiency. Therefore, faster lumen formation led to smaller value of $c_{1/2}$.

Results

Matrix rigidity influences lumen formation

To test how mechanical properties of collagen influence lumen formation, we cultured single YMD cells in collagen gels jellified for 1 or 2 h and examined the changes in efficiency and rate of lumen formation caused by the change in ECM rigidity. Rheometric measurements revealed that two-hour jellification rendered the ECM 1.4 times more rigid. The resulting cumulative probability plots gave a statistical measure of the probability to initiate a lumen within a defined number of cells in the aggregate (Fig. 10, *C* and *D*). Data points were well fitted ($\chi^2 = 0.00083$ for 1 h jellification and $\chi^2 = 0.00495$ for 2 h jellification) by the two-parameter statistical function.

Compared against control YMD samples (1 h jellification, Fig. 10 *C*), lumen formation efficiency is slightly but not significantly reduced ($p = 0.32$; from 96.15 ± 1.66% to 92.69 ± 3.83%) whereas the $c_{1/2}$ is modified to a higher value of statistical significance ($p < 0.1$; from 3.039 ± 0.109 to 3.525 ± 0.350). Thus with the stiffer matrix, lumen initiation tends to occur in aggregates containing 1.15 times more cells, suggesting that lumen formation is delayed by increasing the rigidity of the ECM.

Dr. D. A. Zacharias at the University of Florida is kindly acknowledged for the YMD cells. We thank Dr. Hang Si at WIAS for assistance in using TetGen, and E. DiIorio and C. Sykes for critically reading the manuscript.

This work was supported by the Top Nano 21 Project No. 6358.1 (R.K. and Y.V.) and the Roche Research Foundation (R.K.). We also acknowledge support from the light microscopy center at ETH Zurich, Switzerland.

REFERENCES

1. O'Brien, L. E., M. M. Zegers, and K. E. Mostov. 2002. Opinion: building epithelial architecture: insights from three-dimensional culture models. *Nat. Rev. Mol. Cell Biol.* 3:531–537.
2. Kroschewski, R. 2004. Molecular mechanisms of epithelial polarity: about shapes, forces, and orientation problems. *News Physiol. Sci.* 19:61–66.
3. Weaver, V. M., O. W. Petersen, F. Wang, C. A. Larabell, P. Briand, C. Damsky, and M. J. Bissell. 1997. Reversion of the malignant phenotype of human breast cells in three-dimensional culture and in vivo by integrin blocking antibodies. *J. Cell Biol.* 137:231–245.
4. Debnath, J., S. K. Muthuswamy, and J. S. Brugge. 2003. Morphogenesis and oncogenesis of MCF-10A mammary epithelial acini grown in three-dimensional basement membrane cultures. *Methods.* 30:256–268.
5. Wang, A. Z., G. K. Ojakian, and W. J. Nelson. 1990. Steps in the morphogenesis of a polarized epithelium. I. Uncoupling the roles of cell-cell and cell-substratum contact in establishing plasma membrane polarity in multicellular epithelial (MDCK) cysts. *J. Cell Sci.* 95:137–151.
6. Petroll, W., M. and L. Ma. 2003. Direct, dynamic assessment of cell-matrix interactions inside fibrillar collagen lattices. *Cell Motil. Cytoskeleton.* 55:254–264.
7. Petroll, W. M., H. D. Cavanagh, and J. V. Jester. 2004. Dynamic three-dimensional visualization of collagen matrix remodeling and cytoskeletal organization in living corneal fibroblasts. *Scanning.* 26:1–10.
8. Hardin, J., and T. Walston. 2004. Models of morphogenesis: the mechanisms and mechanics of cell rearrangement. *Curr. Opin. Genet. Dev.* 14:399–406.
9. Sieminski, A. L., R. P. Hebbel, and K. J. Gooch. 2004. The relative magnitudes of endothelial force generation and matrix stiffness modulate capillary morphogenesis in vitro. *Exp. Cell Res.* 297:574–584.
10. Weliky, M., and G. Oster. 1990. The mechanical basis of cell rearrangement. I. Epithelial morphogenesis during Fundulus epiboly. *Development.* 109:373–386.
11. Hsu, S., A. M. Jamieson, and J. Blackwell. 1994. Viscoelastic studies of extracellular matrix interactions in a model native collagen gel system. *Biorheology.* 31:21–36.
12. Kolodney, M. S., and R. B. Wysolmerski. 1992. Isometric contraction by fibroblasts and endothelial cells in tissue culture: a quantitative study. *J. Cell Biol.* 117:73–82.
13. Freyman, T. M., I. V. Yannas, R. Yokoo, and L. J. Gibson. 2002. Fibroblast contractile force is independent of the stiffness which resists the contraction. *Exp. Cell Res.* 272:153–162.
14. Harris, A. K., P. Wild, and D. Stopak. 1980. Silicone rubber substrata: a new wrinkle in the study of cell locomotion. *Science.* 208:177–179.
15. Burton, K., J. H. Park, and D. L. Taylor. 1999. Keratocytes generate traction forces in two phases. *Mol. Biol. Cell.* 10:3745–3769.
16. Dembo, M., and Y. L. Wang. 1999. Stresses at the cell-to-substrate interface during locomotion of fibroblasts. *Biophys. J.* 76:2307–2316.
17. Butler, J. P., I. M. Tolic-Norrelykke, B. Fabry, and J. J. Fredberg. 2002. Traction fields, moments, and strain energy that cells exert on their surroundings. *Am. J. Physiol. Cell Physiol.* 282:C595–C605.
18. Wang, N., E. Ostuni, G. M. Whitesides, and D. E. Ingber. 2002. Micropatterning tractional forces in living cells. *Cell Motil. Cytoskeleton.* 52:97–106.
19. Roy, P., W. M. Petroll, C. J. Chuong, H. D. Cavanagh, and J. V. Jester. 1999. Effect of cell migration on the maintenance of tension on a collagen matrix. *Ann. Biomed. Eng.* 27:721–730.
20. Vanni, S., B. C. Lagerholm, C. Otey, L. D. Taylor, and F. Lanni. 2003. Internet-based image analysis quantifies contractile behavior of individual fibroblasts inside model tissue. *Biophys. J.* 84:2715–2727.
21. Bookstein, F. L. 1991. Morphometric Tools for Landmark Data. Cambridge University Press, Cambridge, UK.
22. Krishnan, L., J. A. Weiss, M. D. Wessman, and J. B. Hoying. 2004. Design and application of a test system for viscoelastic characterization of collagen gels. *Tissue Eng.* 10:241–252.
23. Phan-Thien, N. 2002. Understanding Viscoelasticity: Basics of Rheology. Springer, Berlin, Germany.
24. Fung, Y. C. 1977. Continuum Mechanics. Prentice-Hall, Englewood Cliffs, NJ.
25. Christensen, R. M. 1982. Theory of Viscoelasticity. Academic Press, New York, NY.
26. Tan, J. L., J. Tien, D. M. Pirone, D. S. Gray, K. Bhadriraju, and C. S. Chen. 2003. Cells lying on a bed of microneedles: an approach to isolate mechanical force. *Proc. Natl. Acad. Sci. USA.* 100:1484–1489.
27. Roos, W. H., A. Roth, J. Konle, H. Presting, E. Sackmann, and J. P. Spatz. 2003. Freely suspended actin cortex models on arrays of microfabricated pillars. *ChemPhysChem.* 4:872–877.
28. Brodland, G. W. 2002. The differential interfacial tension hypothesis (DITH): a comprehensive theory for the self-rearrangement of embryonic cells and tissues. *J. Biomech. Eng.* 124:188–197.
29. Honda, H., M. Tanemura, and T. Nagai. 2004. A three-dimensional vertex dynamics cell model of space-filling polyhedra simulating cell behavior in a cell aggregate. *J. Theor. Biol.* 228:147.
30. Palsson, E., and H. G. Othmer. 2000. A model for individual and collective cell movement in Dictyostelium discoideum. *Proc. Natl. Acad. Sci. USA.* 97:10448–10453.
31. Marquez, J. P., G. M. Genin, G. I. Zahalak, and E. L. Elson. 2004. Thin bio-artificial tissues in plane stress: the relationship between cell and tissue strain, and an improved constitutive model. *Biophys. J.*
32. Debnath, J., K. R. Mills, N. L. Collins, M. J. Reginato, S. K. Muthuswamy, and J. S. Brugge. 2002. The role of apoptosis in creating

and maintaining luminal space within normal and oncogene-expressing mammary acini. *Cell.* 111:29–40.

33. Lubarsky, B., and M. A. Krasnow. 2003. Tube morphogenesis: making and shaping biological tubes. *Cell.* 112:19–28.
34. Reference deleted in proof.
35. Kagalwala, F., F. Lanni, and T. Kanade. 2000. Computational model of DIC microscopy for reconstructing 3-D specimens. *Methods Inf. Med.* 39:105–109.
36. Alexopoulos, L. G., G. R. Erickson, and F. Guilak. 2002. A method for quantifying cell size from differential interference contrast images: validation and application to osmotically stressed chondrocytes. *J. Microsc.* 205:125–135.
37. Yu, W., A. Datta, P. Leroy, L. E. O'Brien, G. Mak, T. S. Jou, K. S. Matlin, K. E. Mostov, and M. M. Zegers. 2005. Beta1-integrin orients epithelial polarity via Rac1 and laminin. *Mol. Biol. Cell.* 16:433–445.
38. Wozniak, M. A., R. Desai, P. A. Solski, C. J. Der, and P. J. Keely. 2003. ROCK-generated contractility regulates breast epithelial cell differentiation in response to the physical properties of a three-dimensional collagen matrix. *J. Cell Biol.* 163:583–595.
39. Hayashi, T., and R. W. Carthew. 2004. Surface mechanics mediate pattern formation in the developing retina. *Nature.* 431:647–652.
40. Ojakian, G. K., and R. Schwimmer. 1988. The polarized distribution of an apical cell surface glycoprotein is maintained by interactions with the cytoskeleton of Madin-Darby canine kidney cells. *J. Cell Biol.* 107:2377–2387.
41. Pollack, A. L., R. B. Runyan, and K. E. Mostov. 1998. Morphogenetic mechanisms of epithelial tubulogenesis: MDCK cell polarity is transiently rearranged without loss of cell-cell contact during scatter factor/hepatocyte growth factor-induced tubulogenesis. *Dev. Biol.* 204:64–79.